Two-photon interference : spatial aspects of two-photon entanglement, diffraction, and scattering

Peeters, W.H.

6

Spatial pairing and antipairing of photons in random media

We experimentally demonstrate spatial pairing and spatial antipairing of two entangled photons after propagation through a randomly scattering medium. This two-photon interference phenomenon survives averaging over different realizations of disorder. Despite the random nature of the scattering process, the labeled photons have a natural tendency to cluster together or to avoid each other depending of the symmetry properties of the entanglement. Our experimental results are in excellent agreement with our scattering model based on the random unitary matrix ensemble. The (anti)-pairing behavior is closely related to particle exchange symmetries: pairing for bosonic symmetry, antipairing for fermionic symmetry, and anything in between for anyonic symmetry.

6.1 Introduction

In the previous chapter, we analyzed the spatial structure in individual two-photon speckle patterns. These speckle patterns are visible for single realizations of the scattering medium that is illuminated with a spatially entangled two-photon state. Thus far, we have not yet discussed the scattered two-photon probability density *after* averaging over different realizations of disorder. It is in particular interesting to study the effect of two-photon particle symmetry $A(\mathbf{x}_1, \mathbf{x}_2) = A(\mathbf{x}_2, \mathbf{x}_1)$ on the ensemble-averaged two-photon probability density, since the scattered two-photon probability amplitude needs to obey this symmetry in *each* realization of disorder.

To study the essence of the two-photon symmetry, it is desired to have a physical system that allows tuning of the symmetry properties. In other words, it is desired that there is no particle exchange constraint to $A(\mathbf{x}_1, \mathbf{x}_2)$ at all. To achieve this, we must design the physical system in which photon 1 and photon 2 are labeled, either via their energies or via their polarizations. This labeling relieves the symmetry constraint because the two spatial coordinates of $A(\mathbf{x}_1, \mathbf{x}_2)$ now refer to distinguishable photons that are individually addressable via their energy or polarization. To study how symmetry affects two-photon scattering, the scattering process should not modify the labeling degree of freedom of the photons, and the spatial scatter matrix should be identical for the two photons. These constraints on the scattering process are quite stringent, but, as we shall demonstrate, such a scattering system is experimentally feasible.

In this chapter, we study the ensemble-averaged spatial density matrix of the multiply-scattered entangled photon pair. We find that the probability density contains spatial structure depending on the symmetry properties of the incident photon pair. The two photons exhibit a tendency to cluster together (pairing) for bosonic spatial symmetry or to avoid each other (antipairing) for fermionic spatial symmetry. We use the terminology (anti-)pairing instead of (anti-)bunching, because the two photons never occupy the same optical mode due to their orthogonal labels. In Sec. 6.2 we provide a theoretical model based on the random unitary matrix ensemble. Section 6.3 describes experiments in which photon pairing and antipairing is observed. Finally, Secs. 6.4-6.5 contain a concluding discussion and a discussion on potential future research.

6.2 Random unitary scattering of labeled photons

In this section we provide a basic two-photon scattering model describing photon pairing and antipairing after random unitary propagation. We start with a pure

quasimonochromatic two-photon state

$$|\Psi_{\text{in}}\rangle = \sum_{k=1}^{M}\sum_{l=1}^{M} A_{kl}\hat{a}_k^\dagger \hat{b}_l^\dagger |\text{vac}\rangle, \tag{6.1}$$

where $\hat{a}_i^\dagger$ and $\hat{b}_i^\dagger$ are photon creation operators of photons with identical spatial profiles i but with orthogonal polarization or energy. The number $M \geq 2$ quantifies the dimensionality of the spatial basis for each photon. The two photons are labeled via their polarization or energy. Therefore, we may also write state Eq. (6.1) in particle notation

$$|\Psi_{\text{in}}\rangle = \sum_{k=1}^{M}\sum_{l=1}^{M} A_{kl}|k\rangle_1 \otimes |l\rangle_2, \tag{6.2}$$

where $|k\rangle_1$ denotes the spatial k-state of the photon with label 1, and $|l\rangle_2$ denotes the spatial l-state of the photon with label 2. Normalization of the input state requires

$$\sum_{k=1}^{M}\sum_{l=1}^{M} |A_{kl}|^2 = 1. \tag{6.3}$$

The notation chosen in Eq. (6.2) directly shows how $|\Psi_{\text{in}}\rangle$ can be spatially entangled for properly chosen A_{kl}. State $|\Psi_{\text{in}}\rangle$ is entangled if it is impossible to write Eq. (6.2) in a separable form.

The incident two-photon state will now undergo a quasimonochromatic, linear, and lossless scattering process. We put two extra restrictions on this scattering process:

(1) The spatial scattering process does not affect the labeling property of the photons.
(2) The spatial scattering matrix is identical for the two photons.

Under condition (1), the two photons remain distinguishable via their label throughout the scattering process. By also obeying condition (2), we can use the same unitary (=energy-conserving) spatial scattering matrix u_{ij} for photon 1 and photon 2. We calculate the scattered output state via a coupling of modes formalism

$$\begin{cases} \hat{c}_i = \sum_{j=1}^{M} u_{ij}\hat{a}_j \\ \hat{d}_i = \sum_{j=1}^{M} u_{ij}\hat{b}_j \end{cases} \iff \begin{cases} \hat{a}_j^\dagger = \sum_{i=1}^{M} u_{ij}\hat{c}_i^\dagger \\ \hat{b}_j^\dagger = \sum_{i=1}^{M} u_{ij}\hat{d}_i^\dagger \end{cases} \tag{6.4}$$

where we used unitarity of u_{ij}, and where $\hat{c}_i$ and $\hat{d}_i$ are photon annihilation operators in the output mode space of photon 1 and photon 2, respectively.

By substituting Eq. (6.4) into Eq. (6.1) we obtain the scattered output state

$$|\Psi_{\text{out}}\rangle = \sum_{k=1}^{M}\sum_{l=1}^{M}\sum_{m=1}^{M}\sum_{p=1}^{M} A_{kl}u_{mk}u_{pl}\hat{c}_m^\dagger\hat{d}_p^\dagger|\text{vac}\rangle, \tag{6.5}$$

The aim is to perform averaging over different realizations of disorder. Therefore, it is most suitable to describe the ensemble-averaged scattered light as a mixed state with density operator

$$\hat{\rho}^{(\text{out})} \equiv \overline{|\Psi_{\text{out}}\rangle\langle\Psi_{\text{out}}|}, \tag{6.6}$$

where the bar denotes averaging over different realizations of disorder. For notational convenience we will express the density operator in a density-matrix form

$$\hat{\rho}^{(\text{out})} = \sum_{q=1}^{M}\sum_{r=1}^{M}\sum_{q'=1}^{M}\sum_{r'=1}^{M} \rho^{(\text{out})}_{qr,q'r'}\hat{c}_q^\dagger\hat{d}_r^\dagger|\text{vac}\rangle\langle\text{vac}|\hat{d}_{r'}\hat{c}_{q'} \tag{6.7}$$

$$\rho^{(\text{out})}_{qr,q'r'} = \langle\text{vac}|\hat{d}_r\hat{c}_q\hat{\rho}^{(\text{out})}\hat{c}_{q'}^\dagger\hat{d}_{r'}^\dagger|\text{vac}\rangle, \tag{6.8}$$

where we used the completeness and orthonormality of the two-photon basis states $\hat{c}_q^\dagger\hat{d}_r^\dagger|\text{vac}\rangle$. By combining Eqs. (6.8), (6.6), and (6.5) we find the density matrix of the scattered two-photon state

$$\rho^{(\text{out})}_{qr,q'r'} = \sum_{k=1}^{M}\sum_{l=1}^{M}\sum_{k'=1}^{M}\sum_{l'=1}^{M} A_{kl}A^*_{k'l'}\overline{u_{qk}u_{rl}u^*_{q'k'}u^*_{r'l'}}. \tag{6.9}$$

In order to perform ensemble averaging, we must choose an ensemble of unitary scattering matrices. In many realistic multiple scattering geometries, the matrix ensemble contains several correlations such as enhanced backscattering [42] and universal conductance fluctuations [44]. We will however omit all these correlations by using the random unitary matrix ensemble, also known as the circular unitary ensemble (CUE)*. This ensemble is implicitly defined via invariant integration over the unitary group [147, 148], which means that any integral over the ensemble is not affected by multiplication of the ensemble with any unitary matrix of choice (see Eq. (21) in Ref. [148]). In a sense, the random unitary matrix ensemble is the most random ensemble imaginable, since it remains unchanged after multiplication by any unitary matrix. At this point, the choice of the CUE is useful because it is

* For example, enhanced backscattering is contained in the circular orthogonal ensemble (COE) for the reflection matrix r, which means that $r = UU^T$ with U in the CUE [146]. The circular orthogonal ensemble obeys $\overline{|r_{ii}|^2} = 2\overline{|r_{ij}|^2}$ for $i \neq j$.

likely that any two-photon interference phenomenon surviving this type of ensemble averaging will also survive in realistic scattering geometries.

By using this additional assumption of the random unitary matrix ensemble, we have derived explicit expressions (see Appendix) for the ensemble-averaged scattered two-photon density matrix in Eq. (6.9). We find that the two photons have a tendency to either pair up or to avoid each other, depending on the symmetry properties of the entanglement. The degree of pairing in the output can be quantified in a single ratio

$$\mathcal{F} \equiv \frac{\rho^{(\mathrm{out})}_{11,11}}{\rho^{(\mathrm{out})}_{12,12}}, \tag{6.10}$$

which we will call the *pairing factor*. The pairing factor is the two-photon detection probability observed with two detectors looking into the same spatial channel divided by the two-photon detection probability observed with two detectors looking into different spatial channels. The key result of the calculation in the Appendix is that $\mathcal{F} \in [0, 2]$ is

$$\mathcal{F} = \frac{1+\mathcal{S}}{1+\dfrac{1-\mathcal{S}}{M-1}}, \tag{6.11}$$

where the *symmetry parameter* $\mathcal{S} \in [-1, 1]$ defined as

$$\mathcal{S} \equiv \sum_{k=1}^{M}\sum_{l=1}^{M} A_{kl}A^{*}_{lk}, \tag{6.12}$$

quantifies the degree of spatial symmetry in the incident two-photon state. For large scattering matrices ($M \gg 2$) the pairing factor in Eq. (6.11) reduces to $\mathcal{F} = 1 + \mathcal{S}$.

It is intriguing that the phenomenon of (anti-)pairing survives averaging over the random unitary ensemble. The direct dependence of $\mathcal{F}$ on $\mathcal{S}$ in Eq. (6.11) implies that the symmetry parameter $\mathcal{S}$ is conserved under scattering for any realization of the unitary matrix. We recall that the photons must retain their labeling parameter throughout the scattering process and that the scatter matrix should be identical for both photons. In scattering geometries that do not obey these restrictions, the photons might bunch into the same mode (same energy and polarization), or the two photons could encounter different scattering matrices such that $\mathcal{S}$ is not conserved anymore.

We now discuss four classes of symmetry that could be imposed on coefficients A_{kl} of the incident two-photon state $|\Psi_{\mathrm{in}}\rangle$. These four symmetry classes are listed in Tab. 6.1. Each symmetry class corresponds to a certain symmetry parameter $\mathcal{S}$ and thus to a certain degree of pairing $\mathcal{F}$ via Eq. (6.11). We have denoted the first three symmetries as bosonic, fermionic and anyonic, because of their clear connection with particle exchange symmetries in bosonic, fermionic and anyonic [149]

symmetry name	restriction on A_{kl}	symmetry parameter $\mathcal{S}$
bosonic symmetry	$A_{kl} = A_{lk}$	$\mathcal{S} = 1$
fermionic symmetry	$A_{kl} = -A_{lk}$	$\mathcal{S} = -1$
anyonic symmetry [149]	$A_{k\geq l,l} = e^{i\theta} A_{lk}$	$\mathcal{S} = \cos(\theta)$
zero symmetry	$A_{k\geq l,l} = 0$	$\mathcal{S} = 0$

Table 6.1: Definitions of four classes of symmetries, which can exist in the entangled two-photon state in Eq. (6.1). The symmetry parameter $\mathcal{S}$ is defined in Eq. (6.12). This parameter plays a central role because it is directly related to the pairing factor $\mathcal{F}$ in Eqs. (6.10)-(6.11).

quantum fields. This connection becomes clear in the particle notation of $|\Psi_{\text{in}}\rangle$ in Eq. (6.2). This notation is mathematically equivalent to the first-quantization language*, which can be used for most quantum fields. When using this language for a certain quantum field, one must manually symmetrize the pre-factors to achieve the desired particle exchange symmetry [150]. The symmetry rules for bosonic, fermionic, and anyonic quantum fields, are identical to the restrictions on A_{kl} that are listed in Tab. 6.1. This justifies the names that we have chosen for the different kinds of symmetry in A_{kl}.

If bosonic symmetry is imposed, the labeled photons have a tendency to pair up in the random medium ($\mathcal{S} = 1$ and $\mathcal{F} = 2$). In case of fermionic symmetry, the labeled photons will never scatter into identical spatial mode profiles ($\mathcal{S} = -1$ and $\mathcal{F} = 0$). Remarkably, the labeled photons exhibit similar behavior as true bosons (bunching) or true fermions (antibunching) depending on the imposed class of symmetry. This similarity arises from the full mathematical equivalence between the particle notation of the labeled photons in Eq. (6.2) and the first-quantization language that can be applied to true bosonic and fermionic quantum fields. Interestingly, our labeled photons allow anyonic symmetry as well. For this symmetry, we expect behavior somewhere in between full pairing and full antipairing ($-1 < \mathcal{S} < 1$ and $0 < \mathcal{F} < 2$). Finally, one could also impose no symmetry at all, which we call zero symmetry ($A_{k\geq l,l} = 0$, $\mathcal{S} = 0$, and $\mathcal{F} = 1$). This option mimics scattering of classical particles, where each particle carries an intrinsic identity label.

6.3 Experiments

6.3.1 Experimental scheme

In this section we describe an experimental scheme for the demonstration of two-photon pairing and antipairing of multiply-scattered polarization-labeled photons.

* The first-quantization language is a quantum-mechanical description of elementary particles in terms of wave functions for each particle. This language does not use creation and annihilation operators.

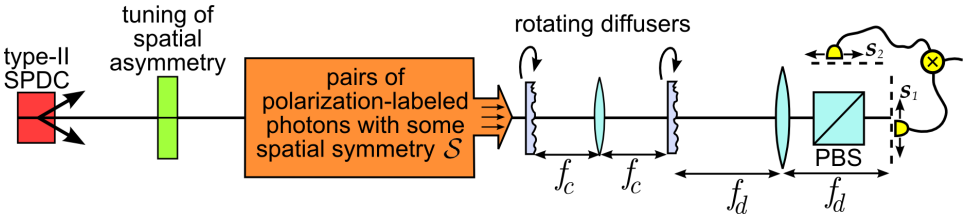

Figure 6.1: Scheme of the experimental process. Polarization-labeled photons are produced via type-II SPDC. The spatial scatter properties of the diffusers are polarization independent, and the diffusers do not affect the polarization. Scattered photons are deterministically separated at a polarizing beam splitter (PBS), detected by independently scanning detectors, and correlated by coincidence logic. Averaging over different realizations of disorder is achieved by fast rotation of the diffusers around the optical axis.

The two-photon interference phenomenon of Eq. (6.11) will be demonstrated for bosonic symmetry ($\mathcal{S} = 1$) and fermionic symmetry ($\mathcal{S} = -1$) in a scattering geometry with a large dimension ($M \gg 2$). The theoretical description is only valid within certain physical conditions of the scattering process. We will address how these conditions are implemented experimentally.

Figure 6.1 schematically depicts the scattering process. The photon pairs are generated via type-II spontaneous parametric down-conversion (SPDC), which produces pairs of polarization-labeled photons [56, 59, 64, 69]. Spatial correlations between the photons arise from conservation of transverse momentum in the down-conversion process. The spatial symmetry parameter $\mathcal{S}$ is tuned by inserting birefringent plates in the far field of the SPDC process (see Sec. 6.3.2 for details*).

In order to demonstrate Eq. (6.11), the scattering process is not allowed to affect the labeling parameter of the photons, which in our case is the polarization. The spatial scattering properties must be identical for both photons. These conditions are met by considering paraxial scattering of diffusers. The random unitary ensemble is approximated with two diffusers positioned in one another's far field and detection in the far field of the second diffuser. Averaging over different realizations of disorder is achieved by relatively fast rotation of the diffusers (see below). The photons are deterministically separated at a beam splitter. The two detectors effectively look at the same spatial profile if the position of detector 2 coincides with the reflected position of detector 1.

* Only the implementation of bosonic and fermionic symmetry is discussed in Sec. 6.3.2. Anyonic symmetry can be straightforwardly implemented by using different wave plates in the anti-symmetrizer in Fig. 6.3. Zero symmetry can be implemented by adding a combination of a polarizer at 45° and a $\lambda/4$-plate at 0° in between the generating crystal and the anti-symmetrizer.

6.3.2 Details of experimental apparatus

The experimental apparatus is schematically depicted in Fig. 6.2. Photon pairs are generated via type-II collinear spontaneous parametric down-conversion (SPDC) in a 5-mm-long periodically poled $KTiOPO_4$ (PPKTP) crystal. The orientation of the crystallographic x, y, and z axes of the PPKTP is indicated in the figure. Down-conversion is operated with a y-polarized pump beam (200 mW at 413.1 nm); the down-converted photons are y and z polarized. Periodic poling is applied along the $\pm z$ axis of the crystal with poling period 11.525 μm along the x axis. The effective nonlinearity, corrected for first-order quasi phase matching, is $(2/\pi)d_{24} = 2.5$ pm/V [111]. This is 4 times less as compared to the nonlinearity in type-I SPDC where the d_{33} of KTP is utilized. Collinear degenerate phase-matching is achieved at $T = 16°$C.

Detection occurs behind narrow band color filters with a full-width-at-half-maximum spectral width of 1 nm around a center wavelength of 826.2 nm. This optical detection bandwidth is below the phase-matching bandwidth* of 1.14 nm. This is required for obtaining an almost spatially pure post-selected two-photon field, after having traced out the subpicosecond structure in its $t_2 - t_1$ coordinate [64]. Spatial purity is required for the generation of high visibility two-photon speckle patterns in experiments with nonrotating diffusers [36]. The spatial properties of the generated two-photon field are practically identical to these of the two-photon field studied in Chapters 4 and 5 because the crystal length, pump beam, and refractive indices are almost identical. Similar two-photon fields have been studied in Refs. [142, 151, 152].

The pump beam is loosely focussed in the crystal-center plane such that the Rayleigh range of the pump beam is much larger than the crystal length (waist $w_p = 160$ μm and Rayleigh range $z_R = \pi w_p^2/\lambda = 20$ cm). Two lenses ($f_a = 200$ mm) in a telescopic configuration directly image the crystal center onto the scattering system.

The scattering system consists of two diffusers that are positioned in one another's far field. Each diffuser is positioned off-center (displaced by 1 cm) such that rotating the diffusers at 15°/s causes good ensemble averaging within the integration time of $12 - 14$ s. Several hundreds of different two-photon speckle spots are being averaged within the integration time of the measurement. The full-width-half-

* The mentioned phase-matching bandwidth $\Delta\lambda = 1.14$ nm is much smaller than the phase-matching bandwidth for type-I SPDC discussed in Chapter 3. This is because the two photons now have orthogonal polarizations and thus propagate with different refractive indices. In the type-II case, the phase-matching bandwidth (FWHM) is calculated from $\Delta\lambda = \lambda_0^2 \Delta\omega/2\pi c$ and the criterion $\mathrm{sinc}^2\left[\frac{L\Delta\omega}{4}\frac{\mathrm{d}}{\mathrm{d}\omega}\left[(n_z(\omega) - n_y(\omega))\omega/c\right]_{\omega=\omega_0}\right] = \frac{1}{2}$, where L is the crystal length, and λ_0 and ω_0 correspond to the vacuum wavelength and angular frequency of a down-converted photon, respectively. The frequency dependent refractive indices of KTP are taken from the Sellmeier dispersion equations in Refs. [106, 107].

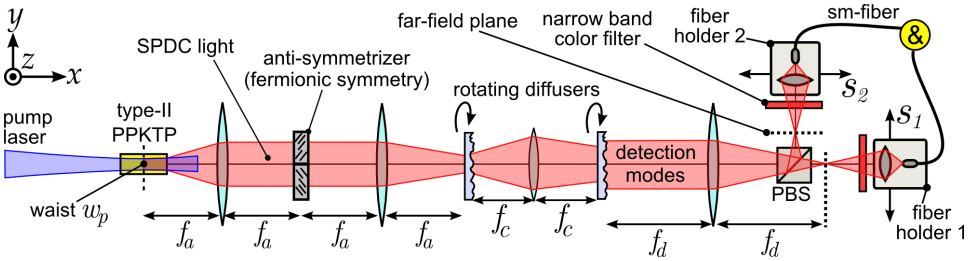

Figure 6.2: Experimental apparatus. Scattered photons are deterministically separated at a polarizing beam splitter (PBS), collected by single mode fibers, and detected by photon counters and coincidence logic. The polarization-labeled photons originate from type-II SPDC having bosonic spatial symmetry. Fermionic spatial symmetry is achieved by adding the anti-symmetrizer (see Fig. 6.3).

maximum scattering angle of each diffuser is 22 mrad. The focal length $f_c = 10$ mm of the lens in between the diffusers is chosen such that the irradiated areas on both diffusers are approximately the same. This is not a strict requirement but merely a convenient choice in relation to the number of speckles and the expected signal to noise ratio.

Behind the scattering system, the two polarization-labeled photons are deterministically separated with a polarizing beam splitter. Detection occurs via projection onto single-mode fibers that are coupled to photon counters and coincidence logic ($\tau_{\text{gate}} = 1.73$ ns). The far-field plane is located in the focal plane of a lens with focal length $f_d = 250$ mm. Spatial resolution in the far-field planes is achieved with tight foci of the detection modes ($w_{\text{det}} = 140$ μm). When the fiber holders are scanned transversely, the detection modes move in their far-field planes but remain fixed in the plane the second diffuser.

An important element of the setup is the "anti-symmetrizer" depicted in Fig. 6.3. When this element is positioned in the far field of the nonlinear crystal it changes the spatial symmetry of the two-photon field from bosonic to fermionic. The anti-symmetrizer consists of two $\lambda/4$-plates closely aligned next to each other (gap is $5 - 15$ μm), and one plate is rotated 90° with respect to the other. The fast and slow axes of the birefringent plates must be oriented parallel to the y and z axes of the coordinate system (defined by the nonlinear crystal). As the photons leave the crystal with approximately opposite transverse momenta, they will generally pass through opposite sides of the anti-symmetrizer. Anti-symmetrization occurs because the phase of the two-photon transmission channel "H-photon left, V-photon right" is $2 \times 90° = 180°$ different from the phase of the two-photon transmission channel "V-photon left, H-photon right". The performance of the anti-symmetrizer is limited by the imperfect angular correlations between the photons, which in turn

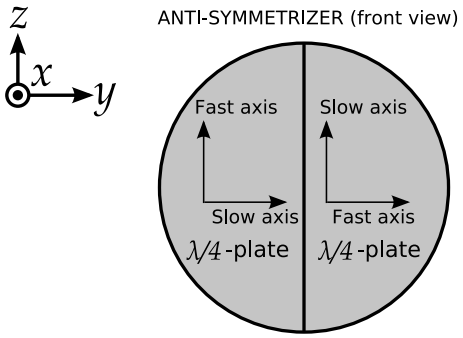

Figure 6.3: Front view of the anti-symmetrizer present in the experimental setup in Fig. 6.2. The orientation in the experimental setup is such that the coordinate system in this figure coincides with the coordinate system in Fig. 6.2.

are limited by the divergence of the pump beam. The probability that both photons pass through the same side must be sufficiently low; the symmetry is only changed when the two photons pass though opposite sides. A very rough estimation of the probability that both photons pass through the same side is $\frac{1}{2}K^{-\frac{1}{2}} = 0.05$, where $K \approx 83$ is the Schmidt number of the entanglement for our source [10]. This limits the symmetry parameter to approximately $\mathcal{S} = 0.95 \times -1 + 0.05 \times 1 = -0.90$.

The element of the anti-symmetrizer is closely related to experimental techniques employed in Refs. [31, 153, 154]. These references use similar birefringent plates in which the polarization state of the entangled light is controlled in a position-dependent fashion. Combining entanglement of two degrees of freedom has already been addressed in all possible combinations: polarization/energy entanglement [155], polarization/transverse-position entanglement [31,74,76,153], and energy/transverse-position entanglement [64]. Combining the entanglement in all three degrees of freedom (polarization, transverse position, and energy) is called hyperentanglement [156, 157].

6.3.3 Experimental results

We have measured the coincidence count rate between two independently-scanning detectors for 2×2 configurations: bosonic and fermionic symmetry, with rotating and nonrotating diffusers for each symmetry. The four recorded two-photon coincidence patterns are displayed in Figs. 6.4(a)-(d). Each data point is recorded with an integration time of $12 - 14$ s, and each pattern takes typically 22 hours to be recorded. All displayed coincidence count rates have been corrected for accidental coincidences, which typically account for 10% of the rawly measured coincidence count rate.

Figures 6.4(a) and (c) display two-photon speckle patterns for bosonic symmetry and fermionic symmetry, respectively. Both patterns show high speckle contrasts, which indicates that the incident two-photon state is spatially pure [36]. Furthermore, both patterns are symmetric with respect to the $s_1 = s_2$ diagonal. This symmetry indicates that the incident two-photon state obeys exchange symmetry (bosonic, fermionic, or anyonic), and that the spatial scatter properties of the scattering system is the same for both photons (polarization independent scattering).

We are mainly interested in what happens on the diagonal $s_1 = s_2$, where both detectors are looking at the same spatial profile. On this diagonal, the relative two-photon speckle intensity is expected to depend on the type of symmetry that is applied. For bosonic symmetry, the two-photon speckle spots on the diagonal are expected to be twice as bright as compared to neighboring speckle spots ($\mathcal{F} = 2$). We indeed observe a couple of remarkably bright two-photon speckle spots on the diagonal of Fig. 6.4(a). For fermionic symmetry, we expect antipairing; not a single speckle spot is allowed to occur on the diagonal ($\mathcal{F} = 0$). We indeed observe complete two-photon darkness on the diagonal of Fig. 6.4(c).

The two-photon interference phenomenon survives averaging over different realizations of disorder. The two-photon speckle patterns are washed out in Figs. 6.4(b) and (d) due to the fast rotation of the diffusers. In the case of bosonic symmetry in figs. 6.4(b), the two-photon intensity on the diagonal clearly stands out. In the case of fermionic symmetry in Fig. 6.4(d), the two photons never occur at the same site.

To quantify the experimental degrees of pairing and antipairing, Fig. 6.5 displays 45°-projections of the ensemble-averaged two-photon patterns. The peak for bosonic symmetry and the dip for fermionic symmetry clearly stand out. The experimental pairing factors are extracted from Gaussian fits through the resulting curves. We obtain $\mathcal{F} = 1.89 \pm 0.05$ and $\mathcal{F} = 0.10 \pm 0.01$ for bosonic symmetry and fermionic symmetry, respectively. Our results clearly demonstrate pairing and antipairing of photons that have propagated through a random medium.

We do not fully understand the observed small deviation from perfect pairing ($\mathcal{F} = 2$) and perfect antipairing ($\mathcal{F} = 0$). Imperfect antipairing might be caused by the fact that a small portion of the photon pairs is transmitted through only one side of the anti-symmetrizer, which will give $\mathcal{S} > -1$ and $\mathcal{F} > 0$ (see Sec. 6.3.2 for details). In the pairing geometry, our experimental realization of a random scatterer (two rotating diffusers) might not correspond to the full ensemble of random matrices, which could cause $\mathcal{F} < 2$. We note that the pairing factor does not depend on the width of the detection modes because the phenomenon of (anti-)pairing is expected to appear in any mode basis. It is though very important that the detection modes of both detectors have practically equal shapes. Any difference between the mode profiles can have a degrading effect on the observed pairing factor. Although

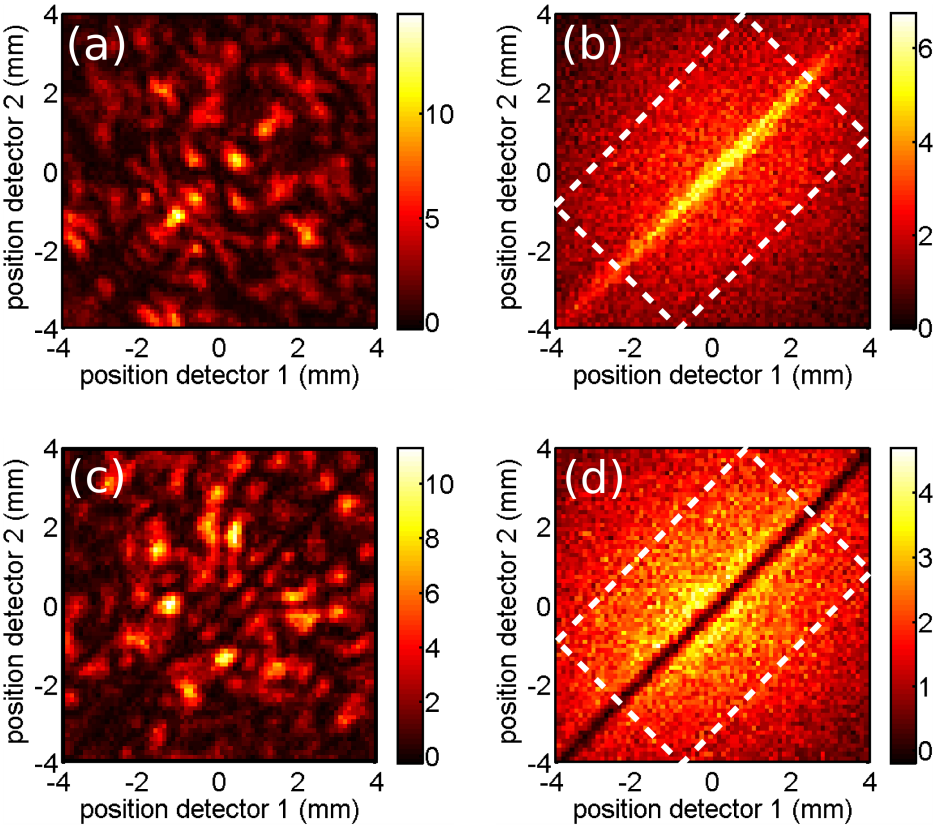

Figure 6.4: Four experimental two-photon patterns for four different configurations: (a) Static random medium and bosonic spatial symmetry. (b) Moving random medium and bosonic spatial symmetry. (c) Static random medium and fermionic spatial symmetry. (d) Moving random medium and fermionic spatial symmetry. The dotted rectangles in panels (b) and (d) indicate the selections that have been used for generating Fig. 6.5.

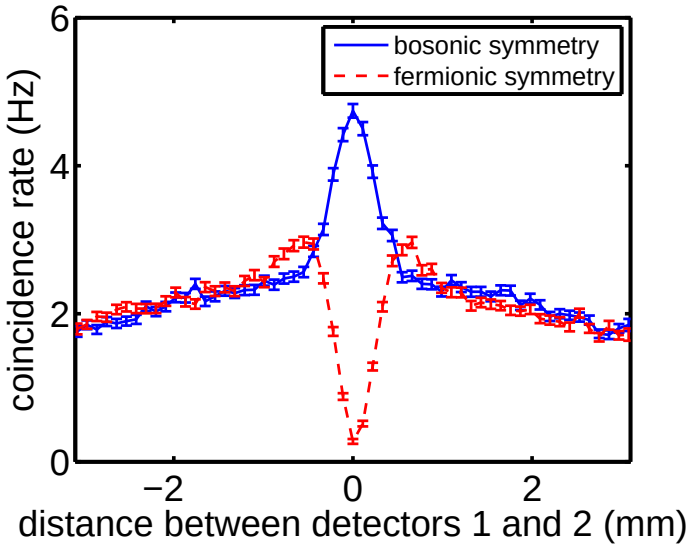

Figure 6.5: Experimental demonstration of pairing for bosonic spatial symmetry and antipairing for fermionic spatial symmetry. This effect has survived ensemble averaging since the random medium was moving fast during recording. These experimental data are extracted from Fig. 6.4 by performing projection operations along the 45° *diagonals within the dotted rectangles.*

we carefully equalized the sizes of our detection modes in the far-field plane, we observed up to 10% differences in divergence and astigmatism (probably caused by limited quality of the fiber tips). This might have had a degrading effect on the observed pairing factors.

We yet have little physical intuition for the physical processes that determine the precise shape of the (anti-)pairing curves in Fig. 6.5. For future reference we note that the FWHM of the peak in the coincidence count rate in Fig. 6.5 is (0.54 ± 0.03) mm. The fermionic dip is somewhat narrower at (0.40 ± 0.02) mm and exhibits small shoulders.

6.4 Concluding discussion

Our scattering experiments with labeled photons demonstrate, for the first time, a (tunable) two-photon interference effect that survives averaging over different re-

alizations of disorder*. It is intriguing to see that some spatial structure survives scattering from rotating diffusers. We have presented a basic theoretical framework underlying the phenomenon. This framework is very effective in explaining the experimental results and is very useful for understanding which experimental parameters are essential. Spatial entanglement plays a central role because, within our theoretical framework, fermionic and anyonic symmetry can not be achieved without entanglement (see Tab. 6.1). The observed effect of (anti-)pairing is a two-photon interference phenomenon since it can be tuned via the phases of the complex two-photon probability amplitudes.

Our scheme provides an experimental toy model that nicely demonstrates the influence of particle exchange symmetries on two-particle propagation. The spatial symmetry between our polarization-labeled photons can be tuned such that it is mathematically equivalent to particle exchange symmetries between indistinguishable (i.e. unlabeled) quantum particles: bosons, fermions and anyons. Our experiments demonstrate how two particles with bosonic exchange symmetry have the tendency to pair up under random unitary scattering. In fermionic symmetry, the particles never come together. Of course, the two photons do not repel each other; it is just that propagation of two fermionic particles to the same site never happens.

Our experiments are closely related to the first observation of spatial antibunching of photons [31]. An observation of spatial antibunching proves nonclassicality of light, but, formally, it is not allowed to use a polarizing beam splitter for such an experiment [31]. We expect that our experimental results would have been qualitatively the same with a normal beam splitter (except for a factor 2 reduction in the coincidence count rate). So if we had used a normal beam splitter, Fig. 6.4(d) would likely have been another observation of spatial antibunching and a proof of nonclassicality of light.

6.5 Outlook

Future research on this two-photon interference phenomenon could address several aspects. First of all, it is desired to get a better understanding of how two-photon (anti-)pairing is related to the geometry of the scattering medium. Currently, we have no theoretical prediction for the shape and widths of the peak and dip in Fig. 6.5. We have little physical intuition for the physical processes that determine the precise shape of these curves.

* Two theoretical papers have recently appeared dealing with two-photon interference effects that survive averaging over different realizations of disorder [37, 38]. Reference [37] studies how Anderson localization in a 1D scatter configuration affects the structure in the ensemble averaged two-photon density for various incident two-photon states. Reference [38] predicts that a two-photon interference phenomenon should appear by itself for sufficiently long randomly scattering wave guides.

Future experiments could address anyonic symmetry to observe pairing factors $0 < \mathcal{F} < 2$. Another interesting option is to observe antipairing with energy-labeled photons. Such a system is particularly interesting because the photons would retain their labeling parameter also in 3D scattering random media. Photons from SPDC are energy-labeled since the total energy of the photon pair is fixed to the photon energy of the pump beam.

It would be very useful to study the phenomenon in scattering systems in which either the labeling of the photons is degraded by the scattering process, or the two photons encounter slightly different scattering matrices. The theoretical formalism must then be extended to a $2M \times 2M$ unitary scattering matrix; the upper-left $M \times M$ submatrix for the first photon, the lower-right submatrix for the second, and the two off-diagonal submatrices for the coupling between the subsystems of the photons.

Finally, it would be interesting to investigate in which way the phenomenon of two-photon (anti-)pairing is related to one-photon interference phenomena. Well-known one-photon interference phenomena that survive averaging over different realizations of disorder are enhanced backscattering and Anderson localization of light [39, 42, 45, 158]. Recent simulations in 1D scattering systems have already shown that profound correlations can exist between (one-photon) Anderson localization and ensemble-averaged two-photon propagation [37].

6.6 Acknowledgements

We thank G. Nienhuis for valuable discussions, and R. D. Gill and S. Zohren for pointing out references on the evaluation of invariant unitary integrals.

6.7 APPENDIX: Scattered density matrix

In this appendix we derive explicit expressions for the scattered two-photon density matrix in Eq. (6.9), recapitulated,

$$\rho^{(\mathrm{out})}_{qr,q'r'} = \sum_{klk'l'} A_{kl} A^*_{k'l'} \overline{u_{qk} u_{rl} u^*_{q'k'} u^*_{r'l'}}. \tag{6.13}$$

The random unitary matrix ensemble will be used for averaging over different realizations of disorder. Any unitary integral of the form

$$\overline{u_{a_1 b_1} \ldots u_{a_n b_n} u^*_{c_1 d_1} \ldots u^*_{c_n d_n}}$$

is nonzero if and only if $\mathbf{c} \in P(\mathbf{a})$ and $\mathbf{d} \in P(\mathbf{b})$, where $P(\mathbf{x})$ is the collection of all different permutations of $\mathbf{x}$, [147, 148]. Logically, there are four essentially different

nonzero second-order integrals possible, being [147,148]

$$\alpha_1 \equiv \overline{u_{11}u_{11}u_{11}^*u_{11}^*} = \frac{2M}{M^2(M+1)}, \tag{6.14}$$

$$\alpha_2 \equiv \overline{u_{11}u_{12}u_{11}^*u_{12}^*} = \frac{M}{M^2(M+1)}, \tag{6.15}$$

$$\alpha_3 \equiv \overline{u_{11}u_{22}u_{11}^*u_{22}^*} = \frac{M^2}{M^2(M+1)(M-1)}, \tag{6.16}$$

$$\alpha_4 \equiv \overline{u_{11}u_{22}u_{12}^*u_{21}^*} = \frac{-M}{M^2(M+1)(M-1)}, \tag{6.17}$$

where M is the dimension of the random unitary matrix. When applying this knowledge to Eq. (6.13) it is found that the density matrix elements can take four different values

$$\rho_{qr,q'r'}^{(\mathrm{out})} = \begin{cases} \sum_{klk'l'} A_{kl}A_{k'l'}^* \overline{u_{qk}u_{ql}u_{qk'}^*u_{ql'}^*} & , q=q'=r=r' \\ \sum_{klk'l'} A_{kl}A_{k'l'}^* \overline{u_{qk}u_{rl}u_{qk'}^*u_{rl'}^*} & , (q=q') \neq (r=r') \\ \sum_{klk'l'} A_{kl}A_{k'l'}^* \overline{u_{qk}u_{rl}u_{rk'}^*u_{ql'}^*} & , (q=r') \neq (r=q') \\ 0 & , \text{elsewhere.} \end{cases} \tag{6.18}$$

Now it is a matter of bookkeeping to perform the summation and using the integrals in Eqs. (6.14)-(6.17). The nonzero contributions in the summations of Eq. (6.18) are listed in Tab. 6.2. By applying this list to Eq. (6.18) we obtain

$$\rho_{qr,q'r'}^{(\mathrm{out})} = \begin{cases} \alpha_1\mathcal{D} + \alpha_2(\mathcal{T}-\mathcal{D}) + \alpha_2(\mathcal{S}-\mathcal{D}) & , q=q'=r=r' \\ \alpha_2\mathcal{D} + \alpha_3(\mathcal{T}-\mathcal{D}) + \alpha_4(\mathcal{S}-\mathcal{D}) & , (q=q') \neq (r=r') \\ \alpha_2\mathcal{D} + \alpha_4(\mathcal{T}-\mathcal{D}) + \alpha_3(\mathcal{S}-\mathcal{D}) & , (q=r') \neq (r=q') \\ 0 & , \text{elsewhere} \end{cases}, \tag{6.19}$$

where we introduced three functionals of the input A_{kl} being

$$\mathcal{T} \equiv \sum_{k=1}^{M}\sum_{l=1}^{M} A_{kl}A_{kl}^* \tag{6.20}$$

$$\mathcal{D} \equiv \sum_{k=1}^{M} A_{kk}A_{kk}^*, \tag{6.21}$$

$$\mathcal{S} \equiv \sum_{k=1}^{M}\sum_{l=1}^{M} A_{kl}A_{lk}^*. \tag{6.22}$$

	$\overline{u_{qk}u_{ql}u^*_{qk'}u^*_{ql'}}$	$\overline{u_{qk}u_{rl}u^*_{qk'}u^*_{rl'}}$	$\overline{u_{qk}u_{rl}u^*_{rk'}u^*_{ql'}}$
$k=l=k'=l'$	α_1	α_2	α_2
$(k=k')\neq(l=l')$	α_2	α_3	α_4
$(k=l')\neq(l=k')$	α_2	α_4	α_3

Table 6.2: Listing of nonzero outcomes for the three unitary integrals in Eq. (6.18) for different combinations of the summation indices k, l, k', and l' (note that $q \neq r$). The coefficients α_i are defined in Eqs. (6.14)-(6.17).

The symbols $\mathcal{T}$, $\mathcal{D} \in [0, \mathcal{T}]$, and $\mathcal{S} \in [-(\mathcal{T}-\mathcal{D}), +(\mathcal{T}-\mathcal{D})]$ stand for *total power*, *diagonal power*, and *symmetry parameter*, respectively.

By substituting Eqs. (6.14)-(6.17) for the unitary integrals α_i in Eq. (6.19) we find

$$\rho^{(\mathrm{out})}_{qr,q'r'} = \begin{cases} \dfrac{1}{M}\left(\dfrac{\mathcal{T}+\mathcal{S}}{M+1}\right) & , q=q'=r=r' \\ \dfrac{1}{M(M-1)}\left(\dfrac{M\mathcal{T}-\mathcal{S}}{M+1}\right) & , (q=q')\neq(r=r') \\ \dfrac{1}{M(M-1)}\left(\dfrac{M\mathcal{S}-\mathcal{T}}{M+1}\right) & , (q=r')\neq(r=q') \\ 0 & , \text{elsewhere} \end{cases} \tag{6.23}$$

We now make two remarks of mathematical interest. The first remark is that $\mathcal{T}$ and $\mathcal{S}$ are functionals of A_{kl} that are conserved under transformation via any unitary scattering matrix. This can easily be demonstrated by combining the appropriate elements of $\rho^{(\mathrm{out})}_{qr,qr}$ to obtain the average $\mathcal{T}$ and $\mathcal{S}$ in the output state being

$$\overline{\mathcal{T}^{(\mathrm{out})}} = \sum_{qr} \rho^{(\mathrm{out})}_{qr,qr} = M\rho^{(\mathrm{out})}_{11,11} + M(M-1)\rho^{(\mathrm{out})}_{12,12} = \mathcal{T}, \tag{6.24}$$

$$\overline{\mathcal{S}^{(\mathrm{out})}} = \sum_{qr} \rho^{(\mathrm{out})}_{qr,rq} = M\rho^{(\mathrm{out})}_{11,11} + M(M-1)\rho^{(\mathrm{out})}_{12,21} = \mathcal{S}. \tag{6.25}$$

The second remark is that the unitary integrals in Eqs. (6.14)-(6.17) are uniquely determined by stating that $\mathcal{T}$ is a conserved quantity for any M and any A_{kl}. In other words, by combining Eqs. (6.24) and (6.19) one retrieves Eqs. (6.14)-(6.17). Actually, the unitary integrals are also uniquely determined by stating that $\mathcal{S}$ is a conserved quantity for any M and any A_{kl}. So by combining Eqs. (6.25) and (6.19) one retrieves Eqs. (6.14)-(6.17) as well.

Finally, we restrict ourselves to $\mathcal{T} = 1$, which corresponds to normalized two-photon quantum states in Eq. (6.1). Furthermore, we concentrate on the on-diagonal elements of the scattered density matrix only. The relative strength of

these elements is given by the ratio

$$\mathcal{F} \equiv \frac{\rho_{11,11}^{(\mathrm{out})}}{\rho_{12,12}^{(\mathrm{out})}} = \frac{1+\mathcal{S}}{1+\dfrac{1-\mathcal{S}}{M-1}}, \tag{6.26}$$

which we will call the *pairing factor*, where $\mathcal{S} \in [-1,1]$ and $\mathcal{F} \in [0,2]$. The pairing factor is the two-photon detection probability observed with two detectors looking into the same spatial channel divided by the two-photon detection probability observed with two detectors looking into different spatial channels. Explicit values for these probabilities are easily retrieved by using

$$\mathrm{Tr}\rho_{qr,q'r'}^{(\mathrm{out})} = M\rho_{11,11}^{(\mathrm{out})} + M(M-1)\rho_{12,12}^{(\mathrm{out})} = 1, \tag{6.27}$$

which is associated with energy-conserving scattering processes.